Journal of Solid State Chemistry 184 (2011) 990–1000

Contents lists available at ScienceDirect

Journal of Solid State Chemistry

journal homepage: www.elsevier.com/locate/jssc

Structural characterization and Curie temperature determination of a sodium strontium niobate ferroelectric nanostructured powder

Silvania Lanfredi [a], Diego H.M. Gênova [a], Iara A.O. Brito [b], Alan R.F. Lima [c], Marcos A.L. Nobre [a,*]

[a] Faculdade de Ciências e Tecnologia, FCT, Univ Estadual Paulista, UNESP, P.O Box 467, Presidente Prudente-SP, Brazil
[b] Instituto de Biociências, Letras e Ciências Exatas, Univ Estadual Paulista. UNESP, P.O Box 6154, São José do Rio Preto-SP, Brazil
[c] Departamento de Química, Univ Estadual de Ponta Grossa, UEPG, Ponta Grossa, PR, Brazil

ARTICLE INFO

Article history:
Received 28 October 2010
Received in revised form
2 February 2011
Accepted 2 March 2011
Available online 10 March 2011

Keywords:
Nanostructured powder
Rietveld method
Infrared spectroscopy
Impedance spectroscopy
Ferroelectric
Curie temperature

ABSTRACT

The Curie temperature and its correlation with the magnitude of the displacement of the niobium atom from the center of [NbO_6] octahedra in $NaSr_2Nb_5O_{15}$ nanostructured powder were investigated. A single powder was prepared by high-energy ball milling. A powder with an average crystallite size of 37 nm was prepared by calcining the precursor at 1423 K. The refinement of the structural parameters was carried out by the Rietveld method. $NaSr_2Nb_5O_{15}$ exhibits tetragonal symmetry with the tungsten bronze structure ($a=b=12.3495$ (6) Å, $c=3.8911$ (2) Å, $V=593.432$ (5) Å^3, and $Z=2$). The site occupancy of the Na^+ and Sr^{2+} cations and the interatomic distances between the niobium and oxygen atoms were derived. The [NbO_6] octahedron undergoes both rotation and tilting depending on the crystallographic site. The Curie temperature of the powder was derived using both the impedance and infrared spectroscopy methods.

1. Introduction

Niobates with a tetragonal tungsten bronze (TTB)-type structure are of great scientific, technical, and industrial interest as materials for laser modulation, frequency multiplicity, and the generation of second harmonics for applications in pyroelectric detectors and piezoelectric transducers [1]. Some polycation ferroelectric oxides are also important for microwave telecommunications involving satellite broadcasting and related devices [2]. In some cases, these materials have the potential to replace members of the classic set of ferroelectric ceramics, such as Pb(Zr,Ti)O_3 (PZT), [(Pb($Mg_{1/3}Nb_{2/3}$)O_3] (PMN), and [(Pb,La)(Zr,Ti)O_3] (PLZT) [3]. Furthermore, dielectric, thermistor, and chemical sensor properties can be expected. In the last few years, alkaline and alkaline earth niobates with TTB-type structures, such as $KSr_2Nb_5O_{15}$, $NaSr_2Nb_5O_{15}$, $KBa_2Nb_5O_{15}$, $NaBa_2Nb_5O_{15}$, and $K_3Li_2Nb_5O_{15}$, have been studied due to the high anisotropy of their crystalline structure [4]. The TTB structure can be considered as a derivative of the classical perovskite structure. It can be described by the chemical formula $(A1)_2(A2)_4C_4Nb_{10}O_{30}$. *A*1, *A*2, and *C* denote different oxygen sites in the crystal structure. The *A*1 cavities have cuboctahedral coordination, the *A*2 cavities have pentacapped pentagonal prismatic coordination, and the *C* cavities have tricapped trigonal prismatic coordination. The cavity size decreases in the following order: $A2 > A1 > C$. In TTB-type compounds, alkaline and/or alkaline-earth metals are located in the *A*1 and *A*2 sites, while only small cations like Li are found in the *C* site [5]. Taking into account the TTB-type structure, a wide variety of cation substitutions is possible. In a broad sense, TTB-type compounds with the $A_6Nb_{10}O_{30}$ formula, where *A*=Sr, Ba, are semiconductor oxides containing Nb^{5+} cations. In a TTB-type structure, the coexistence of cations is favorable in both the tetragonal and pentagonal sites. In some of them, cation repartition disorder has been correlated to relaxer behavior [6]. Among TTB-type oxides, the classical ferroelectric quaternary niobates are of particular relevance.

The size and type of replacement ions at different sites of the structure and the degree of disorder have a significant effect on the dielectric properties. In particular, the Curie temperature (T_C) is influenced by these parameters. In fact, the value of T_C depends on the octahedron distortion [7] because the T_C can be changed by application of hydrostatic pressure, which gives rise to further octahedral distortion [8]. In addition, the crystallite size can affect the domain size, and the degree of cooperation between domains can modify the Curie temperature [9]. As a matter of fact, the method of preparation or synthesis and its macroscopic variables, such as the cooling rate and calcination temperature, can change structural properties such as the space group [10]. Alkali–metal

* Corresponding author. Fax: +55 18 3221 5682.
E-mail address: nobremal@fct.unesp.br (M.A. Nobre).

0022-4596/$ - see front matter © 2011 Elsevier Inc. All rights reserved.
doi:10.1016/j.jssc.2011.03.001

niobate powders are typically prepared via a solid-state reaction. However, this method does not always lead to a homogeneous mixture of starting materials. The synthesis of polycation niobates by chemical methods leads to the simultaneous improvement of the stoichiometry, texture control, chemical homogeneity, phase purity, and other parameters [11]. Recently, powder preparation based on the mechanical mixture of oxide/carbonates by high-energy ball milling has been reported, and this preparation can decrease the size of the precursor to the scale of nanometers [12]. Unfortunately, most of the information on the Curie temperature has been derived from crystals and ceramics with large grain sizes. At present, there is a lack of data on the Curie temperature of powders.

In this work, the spontaneous polarization of a powder of $NaSr_2Nb_5O_{15}$, its correlation with structural characteristics, and $[NbO_6]$ octahedron distortion were analyzed. The lattice parameters and atomic positions of TTB-type $NaSr_2Nb_5O_{15}$ were determined by structure refinement using the Rietveld method. The site occupancy by Na^+ and Sr^{2+} and the interatomic distances between niobium atoms were derived. The Curie temperature was determined using the structural parameters and showed an excellent agreement with the experimental Curie temperature.

2. Experimental procedure

2.1. Synthesis

$NaSr_2Nb_5O_{15}$ nanostructured powder was prepared by the mechanical mixture of oxides via high-energy ball milling (HEBM) [12]. The starting P.A. reagents were hydrated niobium oxide ($Nb_2O_5 \cdot 4\ H_2O$), which were used to prepare the precursor powder.

The preparation was carried out using a HEBM type Attritor (Netzsch) with a milling chamber of zirconium (600 ml) that was cooled with circulation water throughout the process. The mixture of the starting materials was carried out in isopropylic alcohol using stabilized zirconia balls of 1.2 mm in diameter. A powder to ball weight ratio of 1:16 was used. The mixture was agitated with a Molinex-type agitator shaft with eccentric radial disks that accelerated the grinding media, which gave an extra radial impulse during each rotation of the shaft with a motor of 1/3 hp. The milling was performed with a rate of 1200 rpm for 5 h.

After milling the reagents, the material was dried in a glove box with forced air flow at 373 K. Single phase powders were obtained after calcination at 1423 K for 12 h. The precursor was calcined in a tube furnace under an integral oxygen atmosphere. An oxygen flow of 300 mL/min was maintained during a complete thermal cycle. Powder was deagglomerated in agate mortar with a 350-mesh minimum.

The powder was characterized by X-ray diffraction and infrared spectroscopy. A fraction of this powder was uniaxially pressed into pellet form. The green compact was retreated at 1423 K in air for 2 h at a heating rate of 2.0 K/min. A relative density equal to 65% of the theoretical density was reached. The aim of the thermal treatment of the powder compact at the same calcination temperature was to eliminate adsorbed gases on the particle interfaces and release compaction stress. The average crystallite size was assumed to be equal or very close to the average crystallite size of the nanostructured powder. In practice, the development of large domains and further interaction between them is blocked.

Thus, the additional contribution to the dielectrical properties stemming from the cooperative phenomenon assigned to large domains is prevented. Furthermore, the magnitude of the intrinsic defect distribution and microstrain in the crystalline lattice were close to the original ones. Therefore, the Curie temperature of a nanostructured powder might be derived with a high level of confidence via impedance spectroscopy.

2.2. Dielectrical characterization

Dielectric measurements were carried out by impedance spectroscopy. Platinum electrodes were deposited on both faces of the sample with a platinum paste coating (TR-7905—Tanaka). After complete solvent evaporation, the sample was dried at 1073 K for 30 min. Measurements were taken in the frequency range of 5 Hz–13 MHz, with an applied potential of 500 mV using an Impedance Analyzer Alpha N High Resolution Dielectric from Novocontrol GmbH, which was controlled by a personal computer. The sample was placed in a sample holder with a two-electrode configuration. Measurements were taken from room temperature to 700 K in 50-K steps at a heating rate equal to 1.0 K/min in air. A 30-min interval was used prior to thermal stabilization before each measurement. The data were plotted using the complex plane formalism, $Z'(\omega)$ *versus* $Z''(\omega)$, and analyzed with Boukamp's EQUIVCRT software. This program works in an environment developed for equivalent electric circuits based on the fitting of the emittance spectra data [13]. The impedance of a ceramic can be represented by $Z^*(\omega) = Z^*_g(\omega) + Z^*_{gb}(\omega)$, where $Z^*_g(\omega)$ and $Z^*_{gb}(\omega)$ correspond to the impedance of the grain and grain boundary, respectively.

The complex dielectric permittivity, $\varepsilon^*(\omega)$, can be derived from impedance data, $Z^*(\omega)$, $Z^*(\omega) = Z'(\omega) + jZ''(\omega)$, using the following relations:

$$\varepsilon^*(\omega) = (j\omega C_o Z^*)^{-1} = \varepsilon'(\omega) + j\varepsilon''(\omega) \quad (1)$$

where $\varepsilon'(\omega)$ and $\varepsilon''(\omega)$ represent the real and imaginary parts of the permittivity, respectively and C_o is the vacuum capacitance. Both parameters $\varepsilon'(\omega)$ and $\varepsilon''(\omega)$ were extracted from the impedance in a conventional way, according to the following equations:

$$\varepsilon'(\omega) = Z'' / \left(2\pi f \varepsilon_o A |Z|^2\right), \quad (2)$$

$$\varepsilon''(\omega) = Z' / \left(2\pi f \varepsilon_o A |Z|^2\right) \quad (3)$$

where A represents the geometric factor given by the relation S/l and $|Z|^2$ represents the impedance modulus.

2.3. Structural characterization

Chemical bonds were analyzed by infrared spectroscopy (FTIR). The sample was diluted in KBr in a ratio of 1:100. Measurements were carried out with an instrument resolution of 1 cm^{-1} in the range of 1500–400 cm^{-1} for 100 scans using a Fourier transform spectrometer, Model Digilab Excalibur (FTS 3100 HE series). This range is in the mid-infrared, where the characteristic bands assigned to Nb–O bonds appear. A quantitative analysis of the infrared spectrum was carried out by a careful deconvolution of the absorption profiles using a computer-based program (Peak-Fit program) that considers hidden peaks at wavenumbers different from the local maximum in the data stream. This event does not mean that a hidden peak is not discernible. As a matter of fact, a set of peaks is automatically detectable by the spectrometer. The deconvolution procedure can determine the band position with precision to gain further insight into both the position and the intensity of the band. The first IR spectrum was corrected for dark current noises and background using two-point base line corrections. For the fit to be as realistic as possible, bands detected previously from the transmittance spectrum, which are usually composed of some apparent maxima and well developed

shoulders, were used as starting bands during the deconvolution procedure.

For completeness, the deconvolution procedure was applied to the spectrum range between 300 and 1500 cm^{-1}. Further data adjustment used Gaussian functions to adjust each absorption band. The parameter position, full width at half maximum (FWHM) and intensity of each band were adjusted automatically by the program. The adjust routine was based on the minimization of deviations between the experimental and simulated spectra. Peak positions (wavenumbers) detected automatically by the spectrometer were used as an input file. This procedure decreased the number of trials carried out until best fitted data were found.

Structural characterization of the $NaSr_2Nb_5O_{15}$ nanostructured powder was carried out by X-ray diffraction (XRD). A Siemens (model D-5000) diffractometer with Cu-$K\alpha$ radiation ($\lambda = 1.54$ Å) and a graphite monochromator were used. Measurements were carried out over an angular range of $5^\circ \le 2\theta \le 80^\circ$ with a scanning step of 0.02° and a fixed counting time of 10 s. Divergence, scattered and receiving radiation slits were 1°, 1° and 0.2 mm, respectively.

The $NaSr_2Nb_5O_{15}$ structure was refined according to the Rietveld method using the Fullprof program [14]. The parameters and variables adopted during the refinement process were the background coefficients, profile coefficients, histogram scale, lattice parameters, linear absorption coefficients, coordination parameters or oxygen parameters (X), and isothermal parameters for four kinds of atoms (Na, Sr, Nb, and O). The background level was fitted with a five-order polynomial function and the peak shape with a pseudo-Voigt function. The angular dependence of the peak full-width at half-maximum (H) was defined by a function determined by Caglioti et al. [15]. Using the atomic positions derived in the refinement step, the $NaSr_2Nb_5O_{15}$ unit cell was built using the Diamond software package [16]. The average crystallite size (D) and the lattice strain of $NaSr_2Nb_5O_{15}$ of the nanostructured powder were estimated from X-ray diffraction line broadening. The crystallite size was estimated by Scherrer's equation using the Jade 8 Plus software [17]:

$$D = \frac{k\lambda}{\beta \cos\theta} \tag{4}$$

where β is the broadening of the diffraction line measured at half of the maximum intensity, λ is the wavelength (Cu-$K\alpha$), θ is the Bragg angle for a given diffraction, and k is a constant, which is in general equal to 0.9 for powders. The crystallite size was equal to 37 nm. The instrumental broadening effect was eliminated by subtracting the full width at half-maximum (β_o) of a standard sample (SiO_2) from β of the respective Bragg peaks.

The effect of the HEBM (high-energy ball milling) on the crystallite size of the starting powders Na_2CO_3, $SrCO_3$, and $Nb_2O_5 \cdot 4\ H_2O$ was also investigated. The processing parameters were the same ones used in the preparation of the $NaSr_2Nb_5O_{15}$ precursor powder, as described in Section 2.1.

The starting powders were characterized by XRD, as shown in Fig. 1. Diffraction patterns of the set of starting powders showed that the $Nb_2O_5 \cdot 4H_2O$ prior to the attritor milling presented an amorphous character. Table 1 shows a list of the average crystallite sizes of the starting powders before and after the HEBM procedure. According to XRD analysis, Na_2CO_3 and $SrCO_3$ showed a crystalline character with breadth peaks and crystallite sizes equals to 48 and 36 nm, respectively.

The lattice strain was estimated using the Williamson–Hall [18] approach:

$$\beta \frac{\cos(\theta)}{\lambda} = \frac{1}{D} + 4\varepsilon \frac{\sin(\theta)}{\lambda} \tag{5}$$

where D represents the crystallite size and ε represents the lattice strain. The characteristic Williamson–Hall plot corresponds to the graph of $\beta \cos(\theta)/\lambda$ *versus* $4 \sin(\theta)/\lambda$. Here, $4 \sin(\theta)/\lambda$ is on the x-axis. Each point is assigned to a specific diffraction line. After point collection, a linear regression should give a linear fit. The crystalline size was extracted from the y-intercept of the fit. The lattice strain η was extracted from the slope of the fit curve.

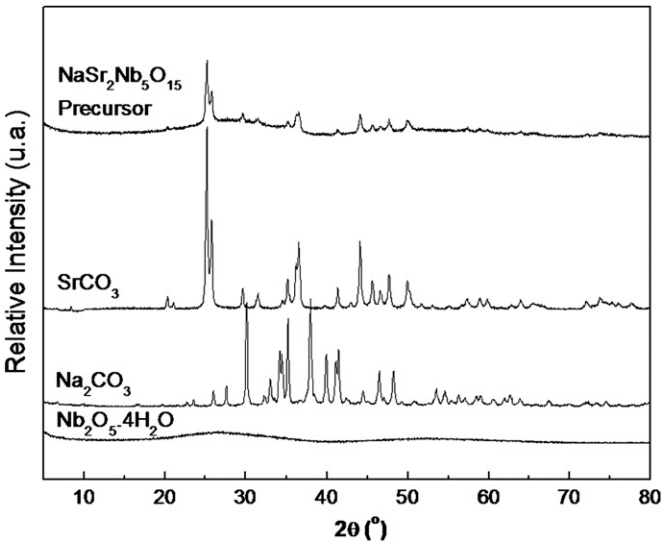

Fig. 1. XRD diffraction patterns of the precursor powders.

Table 1
Average crystallite size (nm) of the precursor powders before and after the milling procedure.

Precursor	Before high energy milling	After high energy milling
Na_2CO_3	58	48
$SrCO_3$	63	36
$Nb_2O_5 \cdot 4H_2O$	Amorphous	Amorphous

3. Results and discussion

3.1. Phase identification

The $NaSr_2Nb_5O_{15}$ nanostructured powder exhibited only a set of diffraction lines ascribed to the TTB-type structure, which was identified from the JCPDS card number 34-0429. A major crystallinity was attained with thermal treatment at 1423 K for 12 h. The crystalline structure exhibited a space group *P4bm* compatible with tetragonal symmetry, as described elsewhere [19]. At the moment, it seems that the preparation route and cooling rate may result in the orthorhombic symmetry type due to cationic disorder (Na, Sr) in the structure [20] and suppression of the phase transition, respectively [21].

Fig. 2 shows the evolution of the average crystallite size (D) and lattice strain (η) of the $NaSr_2Nb_5O_{15}$ nanostructured powder derived as a function of the calcination time. Both the D and η parameters were derived in accordance with Eqs. (4) and (5), respectively. As shown in Fig. 2, the evolution of the average crystallite size and lattice microstrain occurred in several steps. A small increase of the crystallite size was achieved with a decrease in the microstrain lattice as a function of temperature. The lowest average crystallite size, $D = 35$ nm, was observed after 6 h of thermal treatment. Counterclockwise, the highest average crystallite size, at around 37 nm, was derived for the $NaSr_2Nb_5O_{15}$

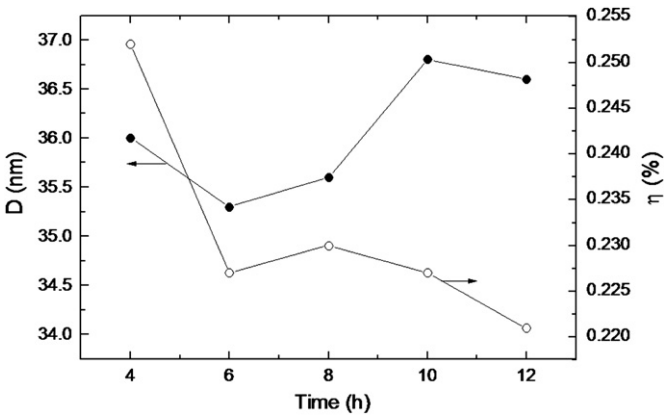

Fig. 2. Average crystallite size and lattice strain as a function of time.

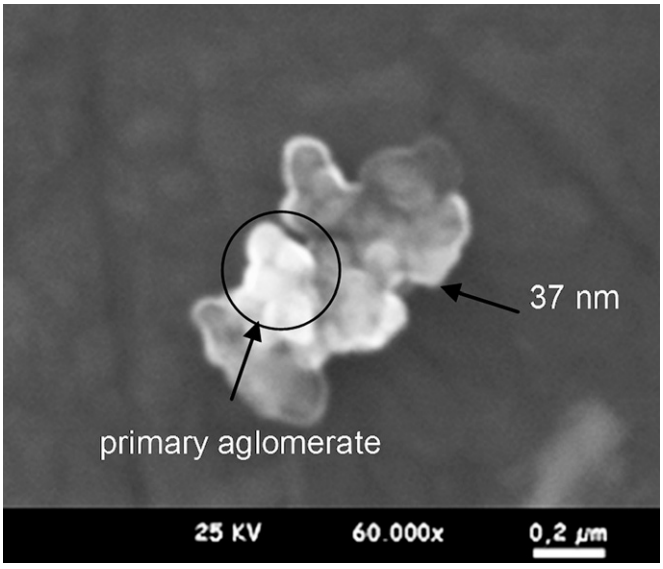

Fig. 3. Scanning electron microscopy (SEM) image of the $NaSr_2Nb_5O_{15}$ precursor powder calcined at 1423 K for 12 h.

precursor powder calcined for 12 h. In this way, the increase of the average crystallite size as a function of thermal treatment time was correlated with the thermal activation of the densifying mechanism (aggregate development) and the non-densifying mechanism (particle growing and agglomerate development) of mass transport at 1423 K. As an example of the non-densifying mechanism, the coalescence of nanoparticles can be related to a lower rate of defect elimination in the material and variations in the degree of microstrain. According to Fig. 2, the mean crystallite size (D) remained nearly constant after the powders were calcined. Such behavior suggests an extensive formation of nanostructures.

The lattice strain of the $NaSr_2Nb_5O_{15}$ precursor powder calcined at 1423 K for 12 h was equal to 0.22, a significant degree.

The size and micro-morphology of the $NaSr_2Nb_5O_{15}$ precursor powder calcined at 1423 K for 12 h was investigated using scanning electron microscopy (SEM), as shown in Fig. 3. The SEM micrography showed spherical particles with several sizes, indicating nanoparticle coalescence and well defined aggregate development. The SEM image shows that the size of primary particles should be of the order of 37 nm because coalescence actuation secondary particles with sizes ranging from 80 to 100 nm were formed. Thus, the XRD and SEM data clearly indicate that ultrafine crystalline $NaSr_2Nb_5O_{15}$ nanostructured powders were prepared. The difference between the crystallite size calculated using X-ray diffraction data and the particle size obtained by SEM was due to the fact that the particles were composed of several crystalline domains, which were observed by X-ray diffraction, while the whole particle was observed in SEM [22].

3.2. Rietveld refinement

The X-ray diffraction pattern was indexed on the basis of a tetragonal unit cell. The structural parameter set of the $NaSr_2Nb_5O_{15}$ nanostructured powders was derived using the Rietveld method. The refinements were performed by taking into account the space groups *P4bm* (No. 100) that are compatible with the rule of existence [$(0\,k\,l)$ $k=2n$] [19]. The powder data and experimental conditions are listed in Table 2. Further theoretical adjustment for the $NaSr_2Nb_5O_{15}$ phase was obtained assuming that each pentagonal site ($4c$ (x, $x+1/2$, z)) was statistically occupied by equal quantities of Na^+ and Sr^{2+} ions and that each tetragonal site ($2a$ ($0\,0\,z$)) was occupied by a Sr^{2+} ion. The trigonal site was considered vacant.

The atomic parameters, isotropic atomic displacement parameters and relative occupancies obtained by the refinement of the $NaSr_2Nb_5O_{15}$ structure are listed in Table 3.

Refinement data obtained for the $NaSr_2Nb_5O_{15}$ precursor powder, which was heated at 1423 K several times for less than 12 h, showed major isotropic atomic displacement parameter B_{eq} values (data not shown). Because the B_{eq} parameter is related to the degree of order–disorder, a higher B_{eq} value suggests a significant degree of disorder in the structure [23]. It is possible to hypothesize that the $NaSr_2Nb_5O_{15}$ powder prepared here exhibited a residual static disorder that is correlated to the *A* and *B* sites occupation and Nb^{5+} cation off-center. This feature is compatible with a process of rearrangement and the growth of crystallites from the sintering of nanostructures [19].

Table 2
Structural data for the $NaSr_2Nb_5O_{15}$ powder and the experimental conditions.

Crystallographic data	
Formula	$NaSr_2Nb_5O_{15}$
Crystal system	Tetragonal
Space group	*P4bm* (No. 100)
a (Å)	12.3495 (6)
c (Å)	3.8911 (2)
V (Å)^3	593.432 (5)
Z	2
Data collection	
Temperature (°C)	26
Wavelength [Cu-$K\alpha$] (Å)	1.5418
Monochromator	Graphite
Measuring range (deg)	$5 \le 2\theta \le 80$
Step ($^\circ$ 2θ)	0.02
Integration time (s)	10
Rietveld data	
Program	FULLPROF
Function for background level	Polynomial—5 order
Function for peak shape	Pseudo-Voigt
($H^2=U\tan^2\theta+V\tan\theta+W$)	
U	0.091759 (4)
V	−0.054645 (2)
W	0.031320 (4)
R_{Bragg} (%)	4.37
R_F (%)	4.28
cR_p (%)	7.44
cR_{wp} (%)	10.8
cR_{exp} (%)	4.98
χ^2	4.67

Table 3
Atomic coordinates, isotropic atomic displacement parameters B_{eq} (Å)^2.

Atoms	Wyckoff position	*x*/*a*	*y*/*b*	*z*/*c*	B_{eq} (Å^2)
Sr(1)	2*a*	0	0	−0.01457 (4)	1.2633 (3)
Na(2)	4*c*	0.17263 (2)	0.67263 (2)	−0.02115 (4)	4.3426 (2)
Sr(2)	4*c*	0.17263 (2)	0.67263 (2)	−0.02115 (4)	4.3426 (2)
Nb(1)	2*b*	0	1/2	1/2	2.6845 (2)
Nb(2)	8*d*	0.07627 (3)	0.21104 (3)	0.47820 (2)	1.0264 (2)
O(1)	8*d*	0.13270 (9)	0.06722 (9)	0.37197 (3)	4.3426 (4)
O(2)	8*d*	0.34232 (1)	0.00469 (8)	0.38305 (4)	4.3426 (4)
O(3)	8*d*	0.08883 (1)	0.19947 (9)	−0.07274 (6)	4.3426 (4)
O(4)	4*c*	0.28409 (8)	0.78409 (8)	0.43520 (9)	4.3426 (4)
O(5)	2*b*	0	1/2	0.02700 (4)	4.3426 (4)

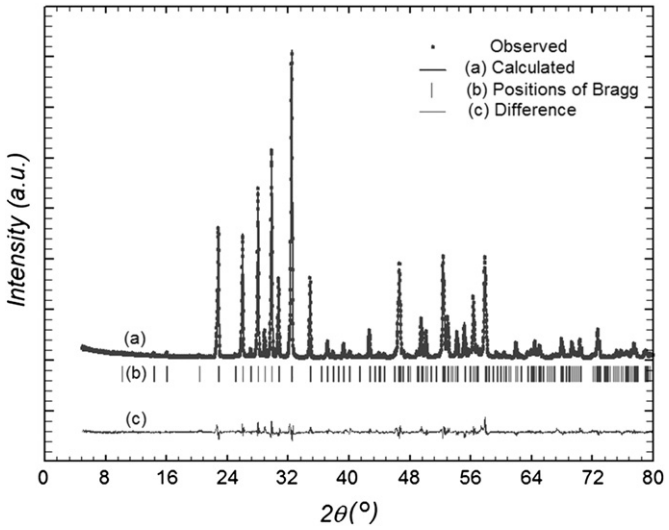

Fig. 4. Rietveld plot for the $NaSr_2Nb_5O_{15}$ powder.

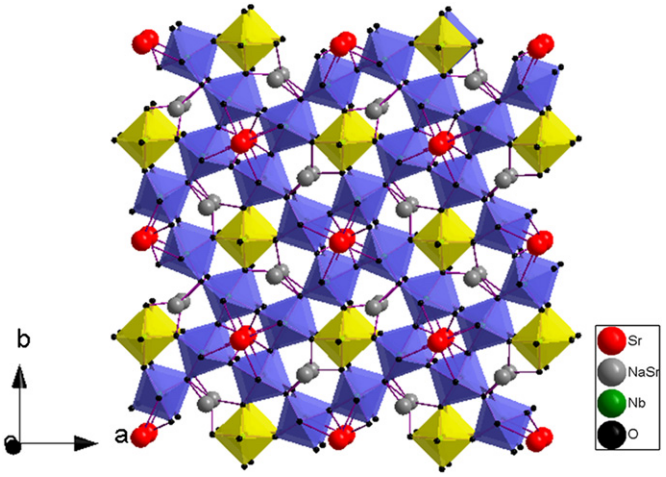

Fig. 5. Graph of the unit cell obtained for the $NaSr_2Nb_5O_{15}$ powder.

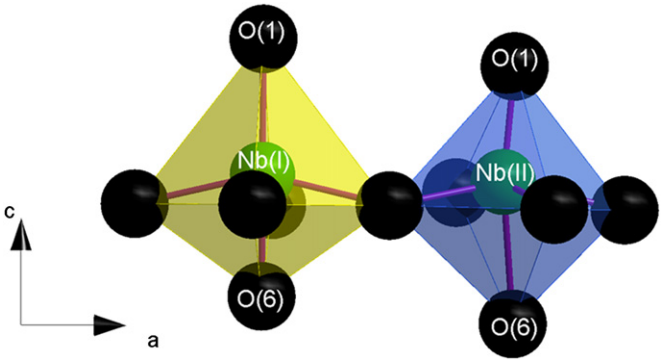

Fig. 6. [Nb(I)O_6] and [Nb(II)O_6] octahedral sites.

The evolution of the crystallite size and lattice microstrain is shown in Fig. 2. An order retrieving has been reported after thermal annealing of the disordered material, in which a large degree of disorder was created by the mechanical refinement of the crystallite size [24], which means that the disorder exhibits a metastable character, being, in essence, a reversible event.

Fig. 4 shows the Rietveld plot for $NaSr_2Nb_5O_{15}$ with the observed and derived X-ray diffraction and their differences. The lattice parameters derived for $NaSr_2Nb_5O_{15}$ were $a=b=$ 12.3495 (6) Å, $c=3.8911$ (2) Å and $V=593.432$ (5) Å^3 in tetragonal symmetry and space group *P4bm* (1 0 0). The tetragonal ratio *c*/*a* was 0.315 with $\sqrt{10}c/a=0.996$. Therefore, in the ferroelectric phase, the TTB cell was not ideal and compressed (*i.e.*, $1>\sqrt{10}c/a$).

Fig. 5 shows the graphic representation of the unit cell obtained for $NaSr_2Nb_5O_{15}$ powder from the data listed in Table 3. Niobium atoms are coordinated to six oxygen atoms, four of which are located, *a priori*, on the same plane as the niobium atoms. The other two are above and below the plane, respectively. This condition is favorable for the formation of an *M* site (octahedron) in the structure [23].

3.3. [NbO_6] Polyhedral distortions analysis

One of the characteristics of TTB-type niobates is the intraoctahedral distortion of the Nb^{5+} cation. The off-center location of the Nb^{5+} cation and octahedral distortion have been attributed to second-order Jahn–Teller (SOJT) effects [25–29] and can be considered as a primary distortion for the cation. Secondary distortions can be further considered and have been attributed to factors as bond networks, lattice stresses in the solid-state framework and punctual defects in the crystalline lattice.

From structural refinement, according to $NaSr_2Nb_5O_{15}$ formula, Nb^{5+} cations can be differentiated as Nb(I) and Nb(II) because they occupy two non-equivalent octahedral sites called *B*1 (2*b* sites) and *B*2 (8*d* sites), as shown in Table 3.

Both [Nb(I)O_6] and [Nb(II)O_6] octahedra are represented in Fig. 6. [NbO_6] octahedra form a three-dimensional rigid framework in the crystal structure. However, the niobium atoms of both types form their own chains based on vertex-shared octahedra [NbO_6]. Chains are linked into the three-dimensional

Table 4
Interatomic distances of Nb–O bonds on the octahedral sites of $NaSr_2Nb_5O_{15}$ powder.

Bonds	Nb–O(1)	Nb^{ξ}–O(2)	Nb^{ξ}–O(3)	Nb^{ξ}–O(4)	Nb^{ξ}–O(5)	Nb–O(6)
[Nb(I)O_6] Octahedra Interatomic distances (Å)	2.0506 (2)	2.0006 (9)	2.0006 (9)	2.0006 (9)	2.0006 (9)	1.8405 (1)
[Nb(II)O_6] Octahedra Interatomic distances (Å)	1.9441 (1)	1.9522 (7)	1.9534 (8)	2.0608 (9)	1.9404 (7)	2.1541 (1)

ξ atoms of the central planes of octahedra.

framework through the oxygen, with Nb atoms located at the off-center positions of octahedra.

Table 4 shows the interatomic distances of the Nb–O bonds in both [Nb(I)O_6] and [Nb(II)O_6] octahedral sites of $NaSr_2Nb_5O_{15}$ nanostructured powder. For the [Nb(I)O_6] octahedron, the four bond lengths of the central plane are equal, while four distinct bond lengths indicates some degree of rotation and tilting in the [Nb(II)O_6] octahedron. Both kinds of octahedra exhibit a cationic displacement from the center of octahedron in the local C_4 direction. This property leads to a short bond-length and a long one for Nb^{5+} cations bonded to apical oxygen. Both [Nb(I)O_6] and [Nb(II)O_6] octahedra showed an increase in the Nb–O (6) bond length related to the oxygen (6) of the apical niobium, as shown in Fig. 6. The Nb–O distance ranged from 1.8405 to 2.0506 Å for Nb(I) and from 1.9441 to 2.1541 Å for Nb(II). The mean Nb–O distances were 1.9822 and 2.0008 Å, respectively.

These values indicate that the Nb–O distances are close to those reported for other TTB-type niobates [30].

The octahedral distortions identified lead to an eventual change in the point group. The ideal point group of the [NbO_6] octahedral is O_h. As pointed out in previous analysis, the [Nb(I)O_6] octahedron shows some degree of distortion, which is based on the apical vertex elongation that leads to a distortion type tetragonal disorder with decreasing octahedron symmetry from the O_h point group to D_{4h}. [Nb(II)O_6] octahedra are more distorted. The Nb–O bond lengths of the Nb(II) constitutes the central plane of the octahedron, termed Nb–O(2), Nb–O(3), Nb–O(4), and Nb–O(5) are different, and such distortion seems to be compatible with some rotation degree along of the *c*-axis. Furthermore, the set of four distinct bond lengths indicates a slight degree of tilting of the octahedron. Therefore, distortions of the [Nb(II)O_6] octahedron involve six vertices. This distortion set can be further characterized as being of type trigonal disorder, which leads to a decrease of the octahedron symmetry from the ideal O_h point group to a new point group, D_{3d}.

Except for some compounds containing La/Ba and K/Sr, the mean distances in the [Nb(II)O_6] octahedra are longer than the mean distances in the [Nb(I)O_6] octahedra, regardless of the valence of the niobium atoms and their partial replacement with transition metal atoms because [Nb(I)O_6] > [Nb(II)O_6] for La/Ba and K/Sr, while [Nb(I)O_6] < [Nb(II)O_6] for the others. In this work, [Nb(I)O_6] < [Nb(II)O_6]. The mean Nb–O length decreases with increasing stretching force constant. Thus, it is possible that the set of normal modes of vibration is distinct for each type of octahedron, as described in Sections 3.2 and 3.4.

3.4. Chemical bond analysis

The number of theoretical reflection bands observed in the TTB structure is very great [31,32].

Because there are few infrared active modes of the internal vibration and due to their partial degeneration, the measured reflection bands of the $NaSr_2Nb_5O_{15}$ are much fewer than those calculated by group theory. In an ideal octahedral anion NbO_6^{-7} with O_h symmetry, there are 15 internal vibrational modes

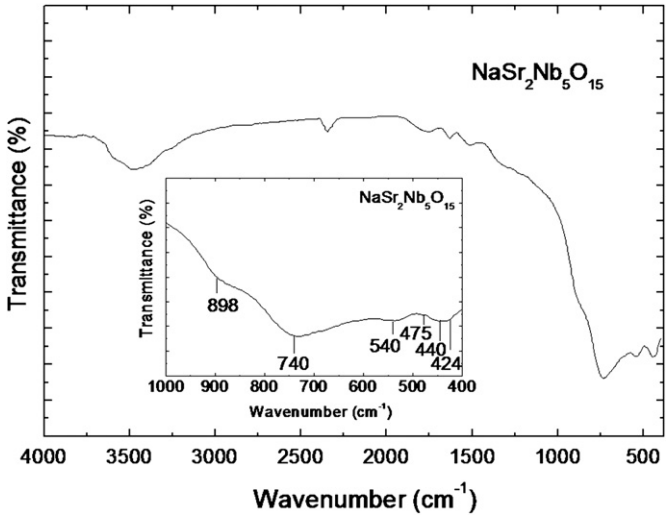

Fig. 7. FT-IR transmittance spectrum of the $NaSr_2Nb_5O_{15}$ powder.

Table 5
Assignment of the FT-IR absorption bands.

Assigments	Wavenumber (cm^{-1})	Intensity	Ref.
Stretching of the Nb–O bonds[a]	475–424	Low	[34,35]
Stretching of the Nb–O bonds[a]	740, 540	Medium	[34,35]
Stretching of the Nb–O bonds[b]	898	Low	[35]

[a] Slightly distorted NbO_6 octahedra.
[b] Distorted NbO_6 octahedra.

($3n-6$, where n is the number of atoms) as follows: $\Gamma_{vib}=A_{1g}(R)+E_g(R)+2T_{1u}(IR)+T_{2g}(R)+T_{2u}$(inactive) [33], where the subscripts g and u represent symmetric and antisymmetric vibrations, respectively. Thus, there might be three strong characteristic vibration bands (infrared) T_{1u} δ(O–Nb–O), T_{1u} ν_{as} (Nb–O) and T_{2u} δ(O–Nb–O), which belong to the internal vibrational modes of the octahedral ions. The O_h symmetry is an over simplification of the infrared vibrational analysis of the octahedral anion NbO_6^{-7} because the Nb^{5+} cation occupies the geometric center of the octahedron counterclockwise, as discussed in Section 3.3. It is important to keep in mind that an octahedron distortion leads to a deviation from O_h symmetry that will result in line broadening and even band splitting as well as change of the number of optically active modes. Because [NbO_6] octahedral are distorted to a different degree, an intensive overlap of peaks is expected, leading to a multi-peak envelop with an irregular shape. A characteristic spectrum of a niobate shows a systematic absence of peaks assigned to particular vibrations.

Fig. 7 shows the FT-IR transmittance spectrum of the $NaSr_2Nb_5O_{15}$ nanostructured powder. It is impossible to obtain further information about the band numbers in the infrared spectrum of the $NaSr_2Nb_5O_{15}$ powder in the region between

400 and 1000 cm^{-1}; see inset. In this region, six bands were typically picked up by the spectrometer software. Bands were positioned between 400 and 900 cm^{-1} as follows: 424, 440, 475, 540, 740, and 898 cm^{-1}. Three of them are centered at 540, 740 and 898 cm^{-1}. Another three bands are sharp and centered at 475, 440 and 424 cm^{-1}. All bands were assigned to Nb–O bonds [34,35]. As a whole, the vibration involving Nb and apical O bonds should give an absorption band at a higher frequency (small wavenumber, $1/\lambda$, or less energetic side of the spectrum) than the Nb–O–Nb bonds of central plane and *vice versa*.

The sharp absorption positioned around 540–424 cm^{-1} and the band centered at 740 cm^{-1} were assigned to Nb–O stretching [34,35]. The band centered at 898 cm^{-1} was assigned to Nb–O stretching of the niobium bond with apical oxygen in the [NbO_6] octahedron [35]. Table 5 lists both the band positions and band characteristics.

The deconvolution of the broad envelop of infrared vibrations should allow further identification of each component. A quantitative analysis of the infrared spectrum was carried out using a curve-fitting technique that separated unresolved IR stretching and bending vibrations based on the Gaussian functions [36–39].

Fig. 8 shows the FT-IR absorption spectrum and theoretical adjustment curve of the $NaSr_2Nb_5O_{15}$ nanostructured powder. As pointed out previously (Section 3.3), both [Nb(I)O_6] and [Nb(II)O_6] octahedra exhibit tetragonal and trigonal disorder, respectively. The point group D_{3d} predicts the appearance of 16 infrared active modes with 7 of A_{2u} and 9 of E_u symmetry [40]. There are eight bands positioned below of 1010 cm^{-1}. All bands exhibit same

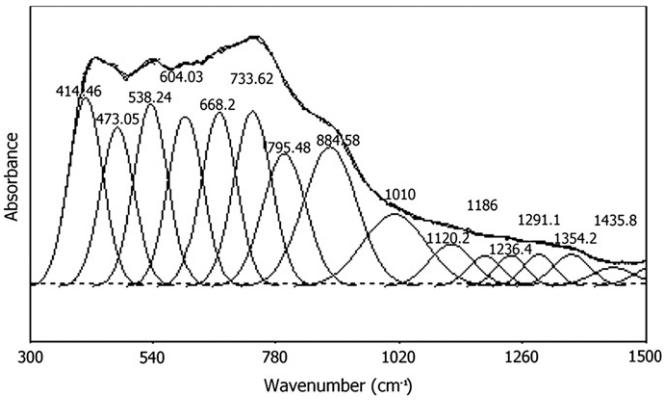

Fig. 8. FT-IR absorbance spectrum and theoretical adjustment from the deconvolution of the spectrum from the set of a Gaussian lineshapes of the $NaSr_2Nb_5O_{15}$ powder.

Table 6
Band center, full width at half maximum (FWHM) and area attained from the deconvoluted peaks of the spectrum of the $NaSr_2Nb_5O_{15}$ powder.

Wavenumber (cm^{-1})	Area	FWHM
414	14	78
473	12	77
538	13	77
604	12	77
668	13	80
733	14	87
795	12	99
884	16	122
1010	10	145
1120	4	101
1186	2	79
1236	2	69
1291	2	72
1354	2	87
1435	2	103
1531	2	112

Correlation factor—(r^2=0.999517).

overlapping degree with their first and second neighboring bands. The band positioned at 440 cm^{-1} was not confirmed by theoretical adjustments; see Fig. 7. All other bands mentioned in the discussion of Fig. 7 have slightly different wavenumbers. Three new bands were derived, in addition to the five mentioned in the discussion of Fig. 7, which are positioned at 604, 668 and 795 cm^{-1}.

Table 6 lists the band centers, full width at half maximum (FWHM) and area attained from the deconvolution of the peaks of the $NaSr_2Nb_5O_{15}$ nanostructured powder spectrum. In the wavenumber range from 300 to 1500 cm^{-1}, eight vibrational bands and eight low intensity bands were identified. The first set of eight vibrations is positioned at a wavenumber lower than 1010 cm^{-1} and contributed 87.9% of the spectrum (envelop observed). One of the bands at 884 cm^{-1} seems to be a linear combination of another two bands: (414+473). The second set of seven small magnitude vibrations with wavenumbers higher than 1010 cm^{-1} contributes only 12.1% of the spectrum.

Except for the vibrations centered at 1120 and 1186 cm^{-1}, all other vibrations seem be a linear combination of other bands. As an example, the vibrations positioned at 1236, 1291, 1354 and 1435 cm^{-1} seem to be the following sums: (414+473+538), (884+414), (884+473) and (414+473+538), respectively. The number of bands derived in the wavenumber range from 400 to 900 cm^{-1} suggests that the vibrations are due to the Nb–O bonds of niobium atoms positioned in non-equivalent crystallographic positions; see the discussion in Section 3.3 and Table 3. According to Fig. 8 and Table 6, the band of highest intensity is centered at 414 cm^{-1}, which exhibits a significant contribution to the envelop spectrum; see the area contribution of this band in Table 6. Based on this double feature and given that [NbO_6] units compose the structural backbone of the $NaSr_2Nb_5O_{15}$ niobate, the characteristics of the band are compatible with a normal mode of vibration of the niobium bond with apical oxygen in the [NbO_6] octahedron. In this sense, the band at 414 cm^{-1} can be assigned to the Nb–O stretching of the niobium bond with apical oxygen in the [NbO_6] octahedron of $NaSr_2Nb_5O_{15}$ nanostructured powder, which represents, *a priori*, the bond correlated to spontaneous polarization, P_S. Here, it should be stressed that, in the tetragonal *P4bm* phases, the polar-axis is along the *c*-axis. In this sense, there is a direct correlation of the magnitude of this vibration with the magnitude of displacement of the Nb location off-center because the force constant of the vibration is directly affected. $NaSr_2Nb_5O_{15}$ with TTB-type structure belongs to the class of ferroelectric niobates has been classified as a displacive ferroelectrics. Here, $NaSr_2Nb_5O_{15}$ with TTB-type structure is considered as a displacive ferroelectric since it involves an orientational order–disorder transition of the Nb^{5+} ion displacements. Thus, the band position corresponding to an internal normal mode of vibration, the stretching of the Nb^{5+} bond, with an apical oxygen of another member of the orientational order–disorder class, can be used as a standard for an estimated value of the wavenumber $\overline{\nu}^{TTB}$, corresponding to the stretching of the Nb^{5+} bond with apical oxygen in the [NbO_6] octahedra of the $NaSr_2Nb_5O_{15}$ structure.

Considering this standard structure, it is a *si ne qua non* condition that the *z*-axis of the [NbO_6] octahedron should be parallel to the *c*-axis of the structure, there is multiplicity of unitary cell *Z* that should be ≥ 2 and that [NbO_6] units form the backbone of the structure. Furthermore, the central plane of the [NbO_6] octahedron is quasi-rigid due to bonding with other [NbO_6] octahedra. In addition, because it is a normal mode, the vibration is not coupled or is weakly coupled to another vibrational mode, which means that the vibration can be considered as quasi-unidimensional. Because the value of vibration assigned to the Nb–O stretching (Nb^{5+} bond with apical oxygen) $\overline{\nu}^{Perovskite}$ of

powder.

$NaNbO_3$ (a classical disordered to orientationally ordered (Nb^{5+} ion displacements) antiferroelectric with [NbO_6] the backbone of structure) is known, it can be used as a standard. This value has been reported as 690 cm^{-1} [34]. Thus, it is sufficient to derive a proper relation between the $\overline{\nu}^{Perovskite}$ and $\overline{\nu}^{TTB}$parameters. This relation can be derived from the classical equation that determines the frequency of vibration of the M–O covalent bond from unidimensional harmonic oscillator theory.

The wavenumber $\overline{\nu}$(nu bar) is defined as the reciprocal of the wavelength:

$$\overline{\nu} = 1/\lambda \tag{6}$$

where $\overline{\nu}$ is in units of cm^{-1} because λ is in units of cm.

The wavelength and frequency, f, are related by Eq. (7):

$$f = c/\lambda \tag{7}$$

where the parameter c represents the speed of light, which is about 3.00×10^{10} cm/s.

A new relation between parameters f and λ is derived by the substitution of Eq. (6) into (7), giving:

$$f = \overline{\nu}c \tag{8}$$

This equation shows a simple relation between the frequency and other trivial parameters involved in the vibration.

The harmonic oscillator was used as a model for the absorption of infrared radiation by covalently ionically bonded solids when the stretching vibration is one normal vibration mode assigned to a specific metal–oxygen bond in an [MeO_6] octahedron. The frequency for a classical unidimensional harmonic oscillator is:

$$f = \frac{1}{2\pi}\sqrt{\frac{K}{\mu}} \tag{9}$$

where K represents the force constant of the bond and μ represents the reduced mass. The reduced mass μ is given by:

$$\frac{1}{\mu} = \frac{1}{m_1} + \frac{1}{m_2} \tag{10}$$

where m_1 and m_2 represent the masses of the bonded atoms.

Combining Eqs. (8) and (9), it is possible to rewrite the wavenumber as a function of the force constant K and reduced mass as:

$$\overline{\nu} = \frac{1}{2\pi c}\sqrt{\frac{K}{\mu}} \tag{11}$$

A simple relation between the wavenumber $\overline{\nu}^{Perovskite}$ of the vibration of the niobium bond with apical oxygen in the [NbO_6] octahedron of $NaNbO_3$ and the wavenumber $\overline{\nu}^{TTB}$ of the vibration of the niobium bond with apical oxygen in $NaSr_2Nb_5O_{15}$ can be derived as follows:

$$\frac{\overline{\nu}^{Perovskite}}{\overline{\nu}^{TTB}} = \sqrt{\frac{K_{perovskite}}{K_{TTB}}} \tag{12}$$

where $K_{perovskite}$ and K_{TTB} correspond to the force constant of Nb–O stretching in the perovskite and TTB structures, respectively. Force constants are explicitly derived by relation (11). The parameter $K_{perovskite}$ is equal to 3.85×10^5 dyn cm^{-1}. This value was derived from the wavenumber of Nb–O stretching in the perovskite, the oxygen mass, and the niobium mass using Eq. (11). Further insight on the force constant along the polar direction can be acquired from infrared spectroscopy data analysis. Classical harmonic oscillator theory should be sufficient. The major focus is on the apical Nb–O bond of the [NbO_6] octahedron. Thus, it is important to derive both the average force constant at the apical Nb–O bond and the reduced mass μ. For atoms in the Nb–O bond, a second expression for μ is obtained by manipulating the expression for μ given by Eq. (10):

$$\mu = \frac{m_{Nb}m_O}{m_{Nb}+m_O} \tag{13}$$

where m_{Nb} and m_O correspond to the mass of the Nb and O atoms, respectively.

Using Eqs. (13) and (11) can be rewritten as:

$$\overline{\nu} = \frac{1}{2\pi c}\sqrt{K\frac{(m_{Nb}+m_O)}{(m_{Nb}\times m_O)}} \tag{14}$$

Eq. (14) describes the physical parameters that influence the stretching frequency of a covalent bond between niobium and apical oxygen, with a reduced mass μ equal to $m_{Nb}\times m_O/m_{Nb}+m_O = 2.27\times10^{-26}$ kg. Then parameters c, π, μ and $\overline{\nu}$ can be substituted into Eq. (14) to derive the force constant K. Therefore, the new parameter K correlated to the TTB structure (K_{TTB}) is equal to 1.38×10^5 dyn cm^{-1}.

Here, $\overline{\nu}^{Perovskite} = 690\,cm^{-1}$ and $\overline{\nu}^{TTB}$ represent the wavenumber to be estimated for the niobium bond with apical oxygen in the $NaSr_2Nb_5O_{15}$ TTB structure. At this point, Eq. (12) can be rewritten as:

$$\overline{\nu}^{TTB} = \frac{1}{\sqrt{\frac{3.85\times10^5\ dyn\,cm^{-1}}{1.38\times10^5\ dyn\,cm^{-1}}}}\overline{\nu}^{Perovskite}, \tag{15}$$

$$\overline{\nu}^{TTB} = 413\,cm^{-1} \tag{16}$$

According to Eq. (16), the wavenumber expected from the vibration of the bond between niobium and apical oxygen in the [NbO_6] octahedron of the $NaSr_2Nb_5O_{15}$ TTB structure is 413 cm^{-1}.

In Eq. (16), the parameter $\overline{\nu}^{TTB}$ is in excellent accordance with the experimental value of 414 cm^{-1}, as described in Section 3.4 and given in the list of values in Table 6. Furthermore, as expected, this band exhibits the highest intensity, according to Fig. 8 and Table 6.

3.5. Spontaneous polarization

$NaSr_2Nb_5O_{15}$ has a *P4bm* space group according to Fig. 4. This space group is noncentrosymmetric, which indicates the development of intrinsic ferroelectricity. In this sense, the magnitude of polarization, called the spontaneous polarization, can be derived from structural parameters. The spontaneous polarization is a function of the displacement of the Nb^{5+} at the center of the [NbO_6] octahedron. The mechanism of development of the spontaneous polarization P_S in the $NaSr_2Nb_5O_{15}$ TTB-type structure is based on the displacement of the "homopolar" Nb metal atom along the polar direction at temperatures lower than the Curie temperature. Intrinsic ferroelectric polarization in niobate oxides is ascribed to the parameter Δz, which gives the magnitude of the displacement of the Nb from the central position of the [NbO_6] octahedron. The value of z (coordinate of Nb (2) at the 8*d* site) is different than $z=1/2$. Taking into account a niobium octahedron, the difference between both niobium oxygen apical lengths [Nb–O(6)–Nb–O(1)] is proportional to twice the niobium off-center displacement Δz along the polar direction at $T \ll T_C$ (Curie temperature) (see Fig. 6). The magnitude of the spontaneous polarization of $NaSr_2Nb_5O_{15}$ P_S depends on the displacement Δz of Nb^{5+} from the center of the [NbO_6] octahedron. It is interesting to note that, in both [Nb(I)O_6] and [Nb(II)O_6] octahedra, the same Δz value of 0.105 Å was observed.

The magnitude of the parameter P_S [41] can be roughly estimated by the following empirical equation:

$$P_S = (258 \pm 9)\Delta z \quad (17)$$

where P_S is given in $\mu C\ cm^{-2}$.

The spontaneous polarization of the $NaSr_2Nb_5O_{15}$ powder was derived using Eq. (17), with the limit value equal to $27.1 \pm 0.945\ \mu C\ cm^{-2}$.

This value is in excellent accordance with the one previously reported for $NaSr_2Nb_5O_{15}$, which was equal to $29\ \mu C\ cm^{-2}$ [8]. It is possible to hypothesize that the increase in the crystallite size and the decrease in the degree of lattice strain should lead to a great spontaneous polarization because ferroelectricity is a cooperative phenomenon. The value of the spontaneous polarization derived here is one order of magnitude higher than the spontaneous polarization value reported for $KSr_2Nb_5O_{15}$, which was approximately $2.5\ \mu C\ cm^{-2}$ [42]. The value of the P_S parameter of $NaSr_2Nb_5O_{15}$ is compatible with those obtained for ferroelectric compounds of the TTB-type structure with space group *P4bm*, such as $Ba_{5/4}Sr_{15/4}Nb_{10}O_{30}$ and $Ba_6Ti_2Nb_8O_{30}$, which present spontaneous polarization values of approximately $25\ \mu C\ cm^{-2}$ [41]. However, such a magnitude of values is expected for single crystals. Recently, the local spontaneous polarization P_S, given in $\mu C\ cm^{-2}$, has been calculated based on the off-center displacement of atoms in the coordination polyhedra by [43]:

$$P_S = (1/v)\sum Z_i \Delta_i \quad (18)$$

where v represents the volume of the unit cell (593.432 Å^3), Δ_i represents the off-center displacement of atoms i (0.105 Å) and Z_i represents the effective charge of atom i, (1.6021×10^{-19} C), respectively. The spontaneous polarization of the $NaSr_2Nb_5O_{15}$ powder was derived from Eq. (18) with a limit value equal to $28.3\ \mu C\ cm^{-2}$.

3.6. Curie temperature analysis

3.6.1. Analysis from dielectric properties

Fig. 9 shows the $NaSr_2Nb_5O_{15}$ impedance diagram at 753 K. The impedance diagram shows two response semicircles. The semicircles are depressed instead of centered on the abscissa axis.

The most accepted approach to interpret semicircle depression is to consider them to be due to a statistical distribution of relaxation times [44]. In the opposite sense, according to Debye's model, a material with a single relaxation time gives an ideal semicircle centered on the abscissa axis. The shape of the diagram suggests that the electrical response is composed of at least two relaxation phenomena with different relaxation frequencies. In addition, both relaxation phenomena obey a non-Debye model, which is further evidence that both of the contributions follow a Cole–Cole type model [45]. Based on previous assumptions, the response $Z^*(\omega)$ was assigned to grain and grain boundary model [44]. These contributions can be simultaneously derived from the theoretical adjustments of the experimental data. In fact, the electric parameters of both the grain and grain boundary interface regions are exact.

An equivalent electric circuit and its respective resistance and capacitance components were derived for $NaSr_2Nb_5O_{15}$ ceramic, as shown in the inset of Fig. 9. The points on the plot represent the experimental data, while the continuous line represents the theoretical adjustment. Excellent agreement between the experimental points and the theoretical curve was obtained. The electrical response is well represented by two equivalent parallel *RC* circuits in series, where *R* represents the resistance and *C* represents the capacitance.

The first contribution (low frequency $< 10^2$ Hz) represents the grain boundary contribution to the electric response. The second one (high frequency $> 10^2$ Hz) corresponds to a specific property of the grain or bulk. The theoretical deconvolution of the electrical response is an alternative approach to derive both contributions [46]. As a consequence, the bulk properties can be unequivocally derived via Boukamp's formalism. In this formalism, the non-ideal character of the polarization phenomenon is represented by a *Q* parameter instead of a *C* parameter. *Q* can be interpreted as a non-ideal capacitance that is physically determined by the parameter Y_o and the exponent n with $n \leq 1$. Y_o tends to approach an ideal capacitance (*C*) when the exponent n tends toward a value of 1.

By hypothesis, the non-ideal character of *Q* is only assigned to a distribution of the relaxation times, which is the origin of the semicircle decentralization observed in Fig. 9. Thus, the parameter $Q(Y_o,n)$ should have an equivalent parameter in the form of an ideal capacitance *C* before it is an adequate interpretation of the electric properties. In Boukamp's formalism, the impedance of a circuit $[RQ(Y_o,n)]$ series is given by:

$$Z^*(\omega) = \frac{R}{1 + RY_o(j\omega)^n} \quad (19)$$

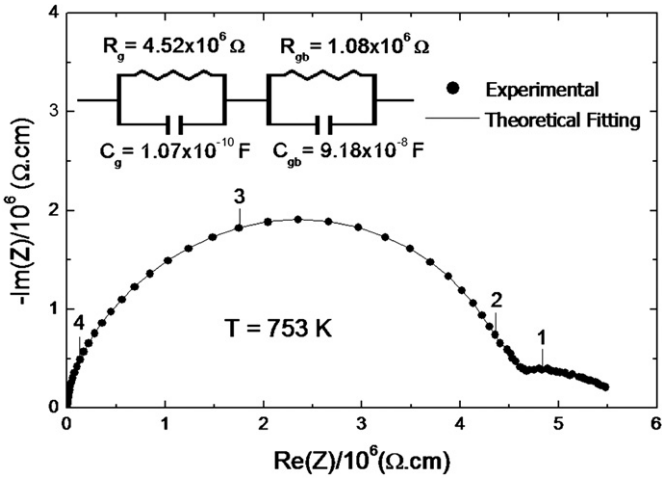

Fig. 9. Experimental and theoretical curves for the $NaSr_2Nb_5O_{15}$ powder with the corresponding equivalent circuit obtained at 753 K. The numbers 1, 2, 3 and 4 give the $\log_{10}$ (signal frequency) for each corresponding point.

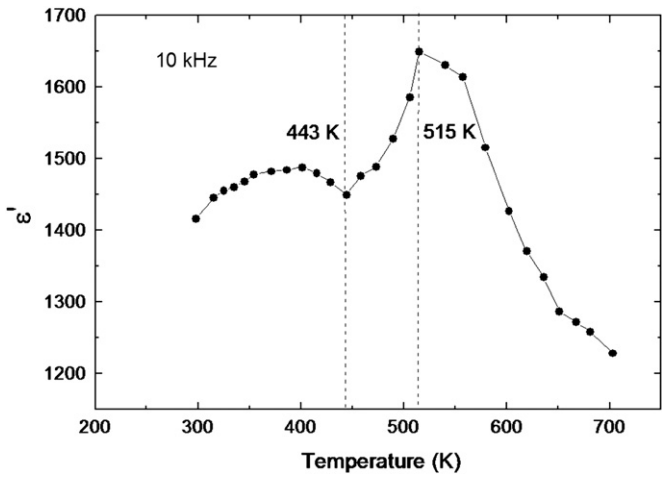

Fig. 10. Relative permittivity, ε′, as a function of temperature of the $NaSr_2Nb_5O_{15}$ powder.

The parameters R, Y_o and n are extracted by theoretical fitting. C is derived from:

$$C = R^{(1-n/n)} Y_o^{(1/n)} \quad (20)$$

In this work, the exponent n is close to unity (quasi-Debye), depending on the measurement temperature. The resistance values derived from the grain and grain boundary of $NaSr_2Nb_5O_{15}$ at 753 K are equal to 4.52×10^6 and $1.08 \times 10^6\ \Omega$, respectively.

The capacitance values of the grain and grain boundary are equal to 1.07×10^{-10} and 9.18×10^{-8} F, respectively. Because the C of the grain is determined, the permittivity ε can be derived from Eq. (21):

$$\varepsilon = \frac{Cl}{\varepsilon_o A} \quad (21)$$

where ε_o is the vacuum permittivity, l is the thickness of the sample and A is the electrode area.

Fig. 10 shows the curve of the dielectric permittivity (ε') of $NaSr_2Nb_5O_{15}$ as a function of temperature, measured at 10 kHz. Each point of this curve was derived using Eq. (2), see Section 2.2. The permittivity curve of $NaSr_2Nb_5O_{15}$ shows a set of anomalies of small intensity occurring in shoulder form at around 298–443 K and a strong and broad polarization peak of high intensity at 515 K, with a permittivity value equal to 1650. Typically, these anomalies have been assigned to phase transitions [9]. Strong anomalies have been assigned to phase transitions involving symmetry changes, while anomalies of small magnitude have been assumed to stem from transitions between space groups [8]. The maximum permittivity was previously assigned to the Curie temperature (T_C=518 K) of $NaSr_2Nb_5O_{15}$ [10]. Thus, the determination of Curie temperature by direct inspection of the permittivity *versus* temperature curve is an imprecise procedure. For the sake of completeness, some anomalies have been reported at temperatures higher than 620 K [10].

Fig. 11 shows the reciprocal permittivity $1/\varepsilon'$ as a function of temperature. Instead of a single experimental curve, the experimental curve allows one to determine two non-parallel linear regions. Each gives a particular Curie temperature value by extrapolation ($1/\varepsilon' \rightarrow 0$). The first curve gives rise to a "Curie temperature" equal to 548 K, which is a value very close to that reported elsewhere [8]. However, the second curve plotted from points above 650 K leads to a "Curie temperature" equal to 230 K. As a matter of fact, one of the previously mentioned Curie temperatures is an apparent value originating from a particular structural evolution as a function of temperature. At temperatures higher than the Curie temperature, the structure should

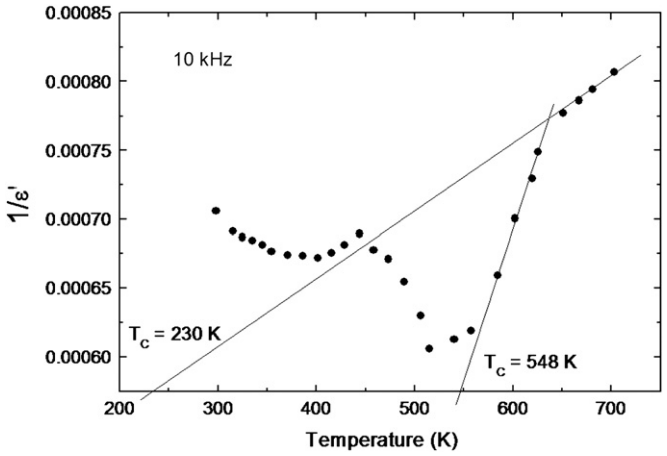

Fig. 11. Reciprocal permittivity, $1/\varepsilon'$, as a function of temperature.

assume a paraelectric state, exhibiting a characteristic centrosymmetric space group corresponding to $P4/mbm$ [23]. However, it appears that Nb^{5+} cations do not occupy the center of the octahedron. The $NaSr_2Nb_5O_{15}$ powder might exhibit a real paraelectric state only at temperatures higher than 651 K, which means that $NaSr_2Nb_5O_{15}$ powder is a displacive ferroelectric material.

As a matter of fact, the $NaSr_2Nb_5O_{15}$ powder undergoes a phase transition from a disordered state to an orientationally ordered material [47].

3.6.2. Analysis from structural properties

The true value of the Curie temperature of $NaSr_2Nb_5O_{15}$ powder can be derived because the value of the displacement of niobium from the center of the octahedron (Δz) was determined (see the discussion in Section 3.5). The temperature of measurement of the Δz parameter should be the same one used to collect the infrared spectrum, as described in Section 3.4. Furthermore, it is important to bear in mind that the polarization occurs parallel to the c-axis (0 0 1) or polar-axis of the $NaSr_2Nb_5O_{15}$ structure. Thus, the parameter Δz should be taken parallel to the polar-axis.

Taking into account that $NaSr_2Nb_5O_{15}$ has ferroelectric behavior due to the displacement of niobium from the octahedron center Δz, the Curie temperature in Kelvin can be derived from the empirical Eq. (22):

$$T_C = (2.00 \pm 0.09) \times 10^4 (\Delta z)^2 \quad (22)$$

where T_C is given in Kelvin and Δz is given in Å.

Eq. (22) has been used successfully to theoretically determine the Curie temperature of a series of displacive ferroelectrics [48]. Here, Δz is equal to 0.105 Å (see the discussion in Section 3.5). The Curie temperature of $NaSr_2Nb_5O_{15}$ powder derived from Eq. (22) is 229 K. This value is in excellent agreement with one of the values derived from the permittivity curve (Fig. 11), which is 230 K. Otherwise, this value seems physically meaningful because, at room temperature ($> T_C$), the TTB $NaSr_2Nb_5O_{15}$ structure should be paraelectric.

Based on the discussion above, the lowest Curie temperature derived here, which is 230 K, should only be an apparent value. Thus, the result derived from the application of Eq. (22) might be due to the use of an inadequate force constant with a value equal to $2.00 \pm 0.09 \times 10^4$.

Therefore, it is necessary to derive a more realistic force constant. The empirical relation in Eq. (22) may be expressed in energy terms [41]:

$$kT_C = \frac{1}{2} K (\Delta z)^2 \quad (23)$$

where k is the Boltzmann constant, which is 1.39×10^{-8} dyn Å K^{-1} (1.39×10^{-23} N m K^{-1}), and K has the dimensions of a force constant. Further simultaneous analysis of Eqs. (22) and (23) shows that the magnitude of this force constant is equal to $5.52 \pm 0.25 \times 10^{-3}$ dyn $Å^{-1}$, which is close to an atomic constant in a crystalline solid. The force constant K can be interpreted as an "average force constant between the homopolar atom and the oxygen framework along the polar direction", as described elsewhere [48]. Thus, the covalent character of the Nb–O bond is relevant to frequency stretching analysis, which is a function of the force constant. The Nb–O bond that exhibits further vibration characteristics should be the bond of the niobium with apical oxygen. Given the [NbO_6] octahedral vibrations, this vibration is expected to exhibit the highest amplitude of vibration, as discussed in Section 3.4.

According to Section 3.4, the new value of the force constant K to describe phenomena at TTB structures is 1.38×10^{-3} dyn $Å^{-1}$ (see derivation details in the discussion in Section 3.4).

Thus, Eq. (22) can be rewritten as:

$$T_C = \frac{K}{2k}(\Delta z)^2 \quad (24)$$

where (K_{TTB}/2 k) represents a new constant called the modified force constant, which is equal to 4.96×10^4 Å^{-2} K. This new value of the modified force constant should substitute for the force constant with a value equal to $2.00 \pm 0.09 \times 10^4$ in Eq. (22). Thus, the newest equation to derive the Curie temperature of a TTB structure can be written as:

$$T_C = (4.96 \times 10^4)(\Delta z)^2 \quad (25)$$

with T_C given in Kelvin and Δz in Å.

Using the equation above, T_C is equal to 546 K, because the Δz derived for the $NaSr_2Nb_5O_{15}$ nanostructured powder, is 0.105 Å (see Section 3.5). Using Eq. (25) and the analysis of Fig. 11, the Curie temperature of the $NaSr_2Nb_5O_{15}$ nanostructured powder prepared was 546 ± 2 K. Eq. (25) is not universal because the modified force constant 4.96×10^4 Å^{-2} K is not a universal constant.

Therefore, the theoretical value of the Curie temperature (546 K), as given by Eq. (25), is in excellent agreement with the value derived experimentally, which is 548 K (see Section 3.6). However, it seems that such a constant can be representative of a group of materials that maintain a set of intrinsic properties and structural features in common. In the $NaNbO_3$ single crystal, at 588 K, the Nb^{5+} cation is off centered in the [NbO_6] octahedron by a displacement (Δz) of 0.11 Å [49]. This value can be substituted into Eq. (25) to derive the Curie temperature of $NaNbO_3$, which is equal to 600.2 K (327.2 °C). Unfortunately, further analysis should be performed using the additional enhancement of the precision in the determination of the Δz parameter. By hypothesis, at $\Delta z = 0.113$ Å, the application of Eq. (25) gives a value of the Curie temperature equal to 663 K (360 °C). This value is very close to one reported for the Curie temperature of $NaNbO_3$ ceramic, which is 361 °C [50].

4. Conclusion

High-energy ball milling is a suitable method for the preparation of single phase niobate powder with nanostructured features and a $NaSr_2Nb_5O_{15}$ TTB-type structure. The unitary cell showed that each pentagonal site is statistically occupied by equal quantities of Na^+ and Sr^{2+} ions and that each tetragonal site is occupied by an Sr^{2+} ion. A high distortion of the [Nb(II)O_6] octahedra occurs due to contributions from both rotation and tilting. The Curie temperature is a function of the magnitude of the parameter displacement of the homopolar atom from the octahedron center and of the average force constant ascribed to the vibration of the homopolar cation in the direction parallel to the polar-axis. The ferroelectric transition in the $NaSr_2Nb_5O_{15}$ powder is of displacive type and involves an orientational order–disorder transition of the Nb^{5+} ion displacements.

Acknowledgments

The authors would like to acknowledge FAPESP, CNPq, and Fundunesp for their financial support.

References

[1] T. Karaki, K. Miyashita, M. Nakatsuji, M. Adachi, Jpn. J. Appl. Phys. 37 (1998) 5277–5279.
[2] D. Kolar, S. Gaberscek, Z. Stadler, D. Suvorov, Ferroelectrics 27 (1980) 269–272.
[3] Y.D. Hou, M.K. Zhu, C.S. Tian, H. Yan, Sensors Actuators A 116 (2004) 455–460.
[4] A. Simon, J. Ravez, Comptes. Rendus. Chimie. 9 (2006) 1268–1276.
[5] S.C. Abrahams, P.B. Jamieson, J.L. Bernstein, J. Chem. Phys. 54 (1971) 2355–2363.
[6] V. Hornebecq, C. Elissalde, F. Weill, A. Villesuzanne, M. Menetrier, J. Ravez, J. Appl. Cryst. 33 (2000) 1037–1045.
[7] J. Ravez, C. R. Acad. Sci. Paris, série II c (1999) 415–419.
[8] M. Lines, A. Glass, Principles and Applications of Ferroelectrics and Related Materials, Oxford, London, 1977.
[9] M.A.L. Nobre, S. Lanfredi, J. Appl. Phys. 93 (2003) 5557–5562.
[10] G.E. García, P.A. Torres, R. Jimenez, C.J.M. Gonzalez, Chem. Mater. 19 (2007) 3575–3580.
[11] Z. Shen, H. Ye, C.L. Mak, K.H. Wong, T.Y. Yum, W. Liu, T. Zou, Mater. Chem. Phys. 99 (2006) 10–14.
[12] S. Lanfredi, L.R. Trindade, A.R. Barros, N.R. Feitosa, M.A.L. Nobre, Cerâmica 51 (2005) 151–156 in portuguese.
[13] B.A. Boukamp, Equivalent Circuit-EQUIVCRT Program-Users Manual, 3, University of Twente, 1989 97.
[14] J.R. Carvajal, An introduction to the Program FullProff 2000, CEA/Saclay, France (2008).
[15] G. Caglioti, A. Paoletti, F.P. Ricci, Nucl. Instrum 3 (1958) 223–228.
[16] DIAMOND, Crystal and Molecular Structure Visualization, Crystal Impact, Inc. 1998–2009.
[17] JADE 8 PLUS, XRD Pattern Processing and Identification Program, Materials Data, Inc. 1995–2007.
[18] G.K. Williamson, W.H. Hall, Acta Met. 1 (1953) 22–31.
[19] S. Lanfredi, C.X. Cardoso, M.A.L. Nobre, Mater. Sci. Eng. 112 (2004) 139–143.
[20] J. Ravez, J.P. Budin, P. Hagenmuller, J. Solid State Chem. 5 (1972) 239–246.
[21] R.J. Xie, Y. Akimune, J. Mater. Chem. 12 (2002) 3156–3161.
[22] C. Vazquez-vazquez, M.C. Blanco, M.A. Lopez-quintela, R.D. Sanchez, J. Rivas, S.B. Oseroff, J. Mater. Chem. 8 (1998) 991–1000.
[23] H. El, A. Belghiti, A. Simon, P. Gravereau, A. Villesuzanne, M. Elaatmani, J. Ravez, Sol. State Sci. 4 (2002) 933–940.
[24] X. Gao, J. Xue, T. Yu, Z. Shen, J. Wang, J. Am. Ceram. Soc. 85 (2002) 833–838.
[25] U. Opik, M.H.L. Pryce, Proc. R. Soc. Lond. A 238 (1957) 425–447.
[26] R.F.W. Bader, Can. J. Chem. 40 (1962) 1164–1175.
[27] R.G. Pearson, J. Am. Chem. Soc. 91 (1969) 4947–4955.
[28] R.A. Wheeler, M.H. Whangbo, T. Hughbanks, R. Hoffmann, J.K. Burdett, T.A. Albright, J. Am. Chem. Soc. 108 (1986) 2222–2236.
[29] K.M. Ok, J. Orzechowski, P.S. Halasyamani, Inorg. Chem. 43 (2004) 964–968.
[30] G. Foulon, M. Ferriol, A. Brenier, G. Boulon, S. Lecocq, Eur. J. Solid State Inorg. Chem. 33 (1996) 673–686.
[31] The International Tables for Crystallography, vol. A: Space-Group Symmetry, Ed. T. Haha, D. Reidel, Publishing Comp. Dordrecht, Boston (1983).
[32] H.R. Xia, H.R. Xia, H.C. Chen, H. Yu, K.X. Wang, B.Y. Zhao, Phys. Status Solidi (b) 210 (1998) 47–59.
[33] H.R. Xia, C.J. Wang, H. Yu, H.C. Chen, Y.Y. Song, Cryst. Res. Technol. 31 (1996) 889–895.
[34] F.J. Farrel, V.A. Maroni, T.G. Spiro, Inorg. Chem. 8 (1969) 2638–2642.
[35] J.M. Jehng, I.E. Wachs, Chem Mater. 3 (1991) 100–107.
[36] C.I. Merzbacher, W.B. White, J. Non-Cryst. Solids 130 (1991) 18–34.
[37] R.D. Husung, R.H. Doremus, J. Mater. Res. 5 (1990) 2209–2217.
[38] Kh.M. Elbadry, F.A. Moustaffa, M.A. Azooz, F.H. Elbatal, Indian J. Pure Appl. Phys. 38 (2000) 741.
[39] E.M.A. Khalil, F.H. Elbatal, Y.M. Hamdy, H.M. Zidan, M.S. Aziz, A.M. Abdelghany, Physica B 405 (2010) 1294–1300.
[40] T. Nagai, M. Sugiyama, M. Sando, K. Niihara, Jpn. J. Appl. Phys. 35 (1996) 5163–5167.
[41] S.C. Abrahams, S.K. Kurtz, P.B. Jamieson, Phys. Rev 172 (1968) 551–553.
[42] S. Alkoyw, C.J. Duran, J. Am. Ceram. Soc. 91 (2008) 1597–1602.
[43] C.L. Jia, S.B. Mi, K. Urban, I. Vrejoiu, M. Alexe, D. Hesse, Phys. Rev. Lett. 102 (2009) 117601–117604.
[44] M.A.L. Nobre, S. Lanfredi, Catalysis Today 78 (2003) 529–538.
[45] K.S. Cole, R.H. Cole, J. Chem. Phys. 9 (1941) 341–351.
[46] S. Lanfredi, M.A.L. Nobre, Appl. Phys. Lett. 81 (2002) 451–453.
[47] O. Hanske-Petitpierre, Y. Yacoby, J. Mustre de Leon, E.A. Stern, J.J. Rehr, Phys. Rev. B 44 (1991) 6700–6707.
[48] P.B. Jamieson, S.C. Abrahams, J.L. Brenstein, J. Chem. Phys. 50 (1969) 4352–4363.
[49] A. Avogadro, G. Bonera, F. Borsa, A. Rigamonti, Phys. Rev. B 9 (1974) 3905–3920.
[50] S. Lanfredi, A.C.M. Rodrigues, L. Dessemond, J. Am. Ceram. Soc. 86 (2003) 2103–2110.